International Journal of Heat and Technology
Vol. 43, No. 6, December, 2025, pp. 2261-2270
Journal homepage: http://iieta.org/journals/ijht

Investigation of Hygrothermal Behavior of Compressed Stabilized Earth Blocks Reinforced with Palm Fibers

Loubna Mouna Djeghri[1*], Azeddine Belhamri[1], Bachir Taallah[2]

[1] Department of HVAC, Laboratoire de Génie Climatique de Constantine (LGCC), Faculty of Sciences and Technology, University Mentouri Constantine 1, Constantine 25017, Algeria
[2] Civil Engineering Research Laboratory, University of Biskra, Biskra 07000, Algeria

Corresponding Author Email: djeghri.loubnamouna@umc.edu.dz

https://doi.org/10.18280/ijht.430624

Received: 16 October 2025
Revised: 17 November 2025
Accepted: 24 November 2025
Available online: 31 December 2025

Keywords:
palm fibers reinforced stabilized compressed earth block, transient heat and mass transfer, experimental characterization, numerical simulation, variable incident solar flux

ABSTRACT

This study established the viability of palm fiber-reinforced compressed stabilized earth blocks (CSEB) for sustainable construction by thoroughly executing a two-step validation process. First, an experimental characterization was carried out to determine the crucial hygrothermal properties of the material (e.g., thermal conductivity, specific heat, porosity), revealing a key interdependence, namely, the thermal parameters were explicitly linked to the moisture content. Second, these moisture-dependent properties were purposely integrated into a transient coupled heat and mass transfer model to simulate the behavior of a simple wall under realistic environmental stresses, including variable solar radiation and convective exchanges. It is noteworthy to say that the results successfully confirmed the noticeable hygrothermal interactions and the combined influence of heat and mass transfer parameters, leading to the strong recommendation that CSEB reinforced with palm fibers be adopted in new bioclimatic housing concepts, especially in rural areas.

1. INTRODUCTION

The global consumption of primary energy is continuously rising due to industrialization and population growth. The residential sector accounts for nearly one-third of this demand and contributes significantly to greenhouse gas emissions [1]. Between 1990 and 2018, the average per capita electricity consumption increased from 2.1 to 3.3 MWh, while Heating, Ventilation, and Air Conditioning (HVAC) systems represented between 16 and 50% of total building energy use [2]. In Algeria, despite short-term energy security based on hydrocarbons, recent national strategies have focused on diversifying the energy mix and improving the thermal efficiency of existing buildings [3, 4]. In this context, studies are currently focused on the development and improvement of the thermal behavior of building materials. The economic and environmental impacts are also key factors influencing this choice. Thus, the environmental footprint of conventional materials in particularly Portland cement, responsible for about 4% of global CO_2 emissions and further aggravated by transportation, has encouraged the adoption of local, low-impact alternatives [5].

In this perspective, earth-based materials, historically adobe, rammed earth, and cob, and more recently compressed stabilized earth blocks (CSEB), offer low embodied energy, high recyclability, and well-documented hygrothermal performance [6, 7]. These properties stem from two main mechanisms: hygroscopicity, which regulates indoor humidity, and thermal inertia, which dampens and delays temperature fluctuations. Furthermore, experimental data for CSEB indicate typical water contents between 2.5 and 4.5% for relative humidity levels from 33% to 75%, as well as vapor permeability favorable to moisture exchange between the wall and indoor air [8, 9]. However, performance remains highly dependent on moisture: as water content increases, the thermal phase shift decreases, although thermal damping remains satisfactory under hot climatic conditions [10].

Quantitatively, Saidi et al. [11] reported that for a CSEB stabilized with 8% cement, moisture content can increase from about 3.7% (dry) to nearly 12% (saturated), while thermal conductivity rises from 0.8014 to 1.11 W/m·K; these variations significantly influence the wall-scale thermal response. In addition, the incorporation of natural fibers has emerged as an effective approach to improve both thermal and hygric transfer properties while enhancing internal cohesion [12, 13]. For example, coconut fibers reduced thermal conductivity from 0.90 to 0.45 W/m·K and increased hygroscopic capacity from 15% to 20% in lateritic blocks [14]. In arid and semi-arid regions, palm fibers stand out for their abundance, low cost, and renewable nature. Although the literature mainly addresses their mechanical performance and steady-state moisture behavior [15, 16], the formulation investigated here, a CSEB containing approximately 0.05% palm fibers, has not yet been evaluated for its transient hygrothermal performance under hot climatic conditions.

The present study aims to analyze, using a combined experimental and numerical approach, the hygrothermal behavior of CSEB incorporating a very low content of date palm fibers (0.05%) [15].

Experimentally, water accessible porosity and capillary

absorption were measured, and thermal properties: Conductivity, diffusivity, specific heat capacity, and effusivity were determined as functions of moisture content to establish the dependencies required for modeling. Numerically, a transient finite volume model with an implicit scheme was implemented. This framework relies on a simplified diffusive coupling that captures the essential interactions between heat and mass fluxes. The resulting spatio-temporal fields of temperature and degree of saturation were simulated through a 0.30 m thick wall, while accounting for convective exchanges at the surfaces. Three representative boundary conditions were analyzed: constant heat flux, periodic flux without solar radiation, and periodic flux with variable solar radiation.

2. MATERIALS AND METHOD

2.1 Tested material

The tested CSEB consisted of 70% soil, 30% fine aggregate crushed sand, 8% cement, and 0.05% date palm fibers [15]. All solid constituents were oven-dried at 70°C for 24 hours to remove residual moisture before mixing. Cement was then added to the initial blending, followed by water, and finally, the fibers were manually incorporated. The blocks are compacted in steel molds with dimensions of 50 × 100 × 200 mm under a pressure of 10 MPa, resulting in prismatic specimens with high density and reduced porosity.

2.2 Experimental characterization at the block scale

The experimental study was conducted at the material scale to characterize the hydrothermal properties of CSEB reinforced with palm fibres. Depending on the type of test, the samples were prepared with specific dimensions and subjected to different moisture content levels. The measured parameters, porosity, thermal conductivity, and thermal diffusivity were used as input data for the numerical model, in order to realistically simulate coupled heat and moisture transfer.

2.2.1 Thermophysical properties characterization

- Thermal conductivity measurement:

Thermal conductivity was measured by applying a unidirectional heat flux through a sample placed between a cold plate and a stable heat source in the EI700 cell [17]. Based on the relationship between the temperatures measured on the hot (T_{hot}) and cold (T_{cool}) sides of the sample and the imposed heat flux (Q), the conductivity is accurately calculated using the following law:

$$\lambda = \frac{(Q - Q_l).e}{(T_{hot} - T_{cool}).A} \tag{1}$$

Ambient and hotbox temperatures are also monitored. To ensure accurate data collection, temperature probes are positioned inside and outside the measurement boxes (Figure 1).

- Thermal diffusivity measurement:

Thermal diffusivity was measured using the flash method [18]: a brief heat pulse of 1000 W, lasting a few seconds, was applied to one face of the specimen, and the temperature on the opposite face was recorded with acquisition software (Figure 2). Under the thermal impulsion, negligible loss assumption, the normalized rear face response follows the classical solution:

$$\frac{T_{Back}}{T_{Max}} = 1 + 2\sum(-1)^n \exp\left(-n^2\pi^2 \frac{\alpha}{e^2} t\right) \tag{2}$$

$t_{1/2}$ is the time at which the rear surface reaches half of the maximum temperature rise. When thermal losses are not negligible, Degiovani's mode [19] estimates the thermal diffusivity from $t_{1/2}$ via an adapted formula and applies corrections based on partial times of the rear face thermogram; the final diffusivity is reported as the average of the corrected estimates:

$$\begin{aligned} \alpha_1 &= \frac{e^2}{t^2_{\frac{5}{6}}}\left(1.15t^2_{\frac{5}{6}} - 1.25t^2_{\frac{2}{3}}\right) \\ a_2 &= \frac{e^2}{t^2_{\frac{5}{6}}}\left(0.761t^2_{\frac{5}{6}} - 0.926t^2_{\frac{1}{2}}\right) \\ a_3 &= \frac{e^2}{t^2_{\frac{5}{6}}}\left(0.618t^2_{\frac{5}{6}} - 0.862t^2_{\frac{1}{3}}\right) \\ a &= \left(\frac{a_1 + a_2 + a_3}{3}\right) \end{aligned} \tag{3}$$

Figure 1. Experimental setup (EI700) measurement cell

Figure 2. Sample preparation: Oven drying and pretest conditioning

- Investigation of the impact of moisture on thermal properties:

For the tests, prismatic samples with dimensions of 200 × 100 × 50 mm were oven dried at 70°C until reaching constant mass (Figure 2). The specimens were then immersed in water to achieve different moisture contents, ranging from dry to

fully saturated states. At each absorption step, the samples were removed, wiped gently to eliminate excess surface water, and immediately weighed with a precision of 0.1 g. Moisture content was calculated using Eq. (4), based on the mass difference relative to the dry mass.

$$w = \frac{m_h}{m_s} = \frac{m^* - m_s}{m_s} \tag{4}$$

2.2.2 Hygric properties characterization

1. Capillary water absorption

Capillary absorption tests were carried out on a full-scale CSEB in order to obtain representative results. The dry mass was obtained after drying at 70°C until a constant weight was achieved. The four side faces of the specimens have been cooled and covered on their four lateral sides to ensure unidirectional flow, with the upper face exposed to air and the lower face immersed in a 5 ± 1 mm water layer to initiate capillary suction. At regular intervals, the sample was removed, dried, and weighed (±0.1 g) (Figure 3). The water absorption per unit area was plotted as a function of √t, and the capillary absorption coefficient ($kg \cdot m^{-2} \cdot s^{-0.5}$) was determined by linear regression in accordance with standard NF EN 1580115801, using the relation:

Function of √t, and the capillary absorption coefficient ($kg \cdot m^{-2}.s^{-0.5}$) was determined by linear regression in accordance with standard NF EN 1580115801, using the relation:

$$a = \frac{m_h - m_s}{\mathrm{A} \times \sqrt{t}} \tag{5}$$

The capillary moisture content ($kg \cdot m^{-3}$) was calculated from the saturated mass and volume of the sample as follows:

$$\mathrm{w}_f = \frac{\mathrm{m_{sat}}}{\mathrm{L} \times \mathrm{l} \times \mathrm{e}} \tag{6}$$

where, m_{sat} is the mass of the sample at saturation (kg), L, l, and e are the dimensions of the sample (m).

Figure 3. Water capillarity test

2.3 Hygrothermal transfer modeling at the wall scale

To illustrate the transient hygrothermal behavior of the CSEB wall, a coupled heat and moisture transfer model is used, based on the theoretical formulation of Philip and De Vries [20]. This one-dimensional model is based on the principle of a rigid and homogeneous porous medium, taking into account the mutual interaction between temperature and moisture fields. The influencing factors are temperature for heat transfer and saturation for moisture migration, with the interaction occurring through temperature-dependent vapor pressure and moisture-dependent transport properties.

The following assumptions are adopted [21]:

- The solid matrix of the porous medium is homogeneous, undeformable, and isotropic.
- The different phases are in thermal and hygroscopic equilibrium.
- Heat and moisture transfers are described at a macroscopic scale.
- Adsorption and desorption hysteresis are assumed to be negligible.
- Phase change during transfer, as well as latent heat effects or chemical reactions, are neglected.
- No chemical reactions occur.
- The density of the liquid phase is constant.
- The interactions between phases are negligible.
- The gaseous phase obeys the ideal gas law.
- The total pressure of the gaseous phase is uniform and constant within the porous medium.
- Heat transfer by radiation is negligible.

Under these assumptions, the governing heat equation, derived from Fourier's law, describes the heat transfer, while the governing mass diffusion equation represents the mass transfer, both occurring through the wall:

The governing heat equation, which describes mass transfer, is given by:

$$\rho Cp \frac{\partial T}{\partial t} = \frac{\partial}{\partial x}\left[\lambda \frac{\partial T}{\partial x}\right] \tag{7}$$

The governing mass equation, which describes mass transfer, is given by:

$$\frac{\partial S}{\partial t} = \frac{\partial}{\partial x}\left[D \frac{\partial S}{\partial x}\right] \tag{8}$$

where, S is the degree of saturation, and $D(S)$ is the saturation dependent moisture diffusivity (m^2/s).

At initial conditions at initial time ($t = 0$ and $0 \le x \le e$):

$$T = T_0 = 293 \text{ K}, S = S_0 = 1$$

The associated boundary conditions are illustrated in Figure 4.

At the boundaries, the temperatures follow a mixed flux condition.

$$(\mathrm{x} = 0); \lambda \left.\frac{\partial T}{\partial t}\right|_{x=0} = hi(T(0) - Ti) \tag{9}$$

$$(\mathrm{x} = \mathrm{e}); -\lambda \left.\frac{\partial T}{\partial t}\right|_{\mathrm{x=e}} = he(T(e) - Te) \tag{10}$$

Moisture exchange at the boundaries is modeled using Neumann-type imposed fluxes:

$$(\mathrm{x} = 0); qmi = hmi(\rho fi - \rho sufi) \tag{11}$$

$$(\mathrm{x}=\mathrm{e}); q_{me}=h_{me}\left(\rho_{\mathrm{sufe}}-\rho_{fe}\right) \tag{12}$$

$$P_v V=nRT=P_v M_v \Rightarrow \rho RT \Rightarrow \frac{PM_v}{RT} \tag{13}$$

The vapor pressure is expressed as follows [22]:

$$P_{v,sat}=9.81\times10^4 10^{\left(5.978-\frac{2225}{T}\right)} \tag{14}$$

and the vapor pressure is given by:

$$P_v=P_{v,sat}\varphi \tag{15}$$

Determining the mass flux requires knowledge of the mass transfer coefficient, hm, which, depending on various physical parameters, can be either calculated or obtained from tables based on wall orientation and the direction of mass flux [23]:

$$h_m=\frac{ShD}{L} \tag{16}$$

At the boundary conditions, the variation of saturation as a function of time is given by:

$$-\rho_L D\left.\frac{\partial S}{\partial x}\right|_{\mathrm{x}=0}=q_{mi} \tag{17}$$

$$\rho_L D\left.\frac{\partial S}{\partial x}\right|_{\mathrm{x}=\mathrm{e}}=q_{me} \tag{18}$$

Applying the same algorithm while accounting for periodic variations in solar heat flux and ambient temperature, the exterior boundary imposes a time-dependent heat flux $\Phi(t)$ at the facade. To simulate realistic summer climatic conditions, this forcing represents the diurnal solar load and updates the surface heat balance as follows:

$$\rho Cp\frac{\partial T}{\partial t}=\frac{\partial}{\partial x}\left[\lambda\frac{\partial T}{\partial x}\right]-\Phi(t) \tag{19}$$

This formulation serves as the foundation for the numerical implementation that follows, capturing the thermal response of the CSEB wall to realistic environmental excitations.

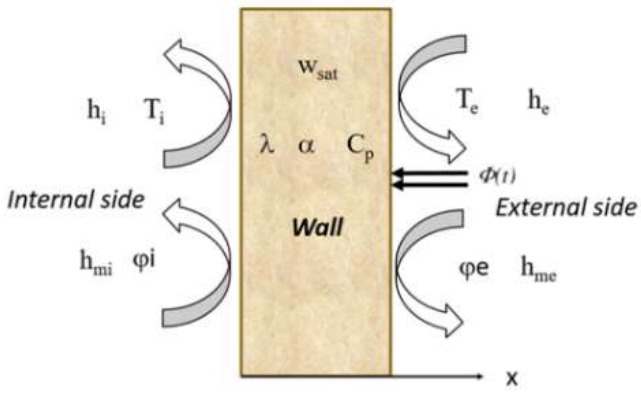

Figure 4. Presentation of the system

2.4 Numerical resolution of the model

The transient simulation used the finite volume method with an implicit scheme and TDMA solver [24], with convergence set at a relative error below 10^{-6}. Moreover, a uniform set of initial conditions ensured consistent comparison across scenarios. For validation, 0.05% palm fiber-reinforced (CSEB) were tested under realistic hot climate conditions. The simulations concerned a 30 cm thick vertical wall with three boundary cases: Constant, periodic without solar flux, and periodic with solar flux. In terms of boundary conditions, heat transfer followed mixed (convective) conditions, while moisture transfer was governed by vapor pressure gradients. Specifically, the external temperature varied as:

$$T_e(t)=T_0+\Delta T\sin(\omega t) \tag{20}$$

Parameters for periodic boundary conditions [25]:

$$T_e=293+15\sin((2\pi t/24))$$

$\omega=2\pi/\tau$, $\tau=24$ h, $T_0=293$ K; and $\Delta T=15$ K.

The solar flux follows a periodic variation: it is zero at night and gradually increases during the day. This variation is expressed by the following equations:

$$\begin{cases}\Phi(t)=\Phi_0\sin(\omega t) & if\ 0\le t\le\tau/2\\ 0 & if\ \tau\le t\le\tau/2\end{cases} \tag{21}$$

The model expresses thermal conductivity as a function of degree of saturation, whereas the experimental data are given in terms of moisture content. The conversion is carried out using the material porosity (ε) according to the relation (22):

$$S=\frac{w}{\varepsilon} \tag{22}$$

The effective thermal conductivity is then prescribed as:

$$\lambda^*(S)=0.279S+0.52 \tag{23}$$

In the absence of measured diffusivity data, $D(S)$ for the CSEB under study, the relation [26] is employed, its use justified by micro-structural proximity to the reference concrete:

$$D(S)=3.22\ \ 10^{-10}\exp(6S) \tag{24}$$

Table 1. Input parameters of the numerical model

Input Parameter for Model	Value
Density (ρ)	2040 kg·m^3
Specific heat capacity (Cp)	993 J·kg·K
External temperature (Te)	313 K
Interior temperature (Ti)	293 K
Internal convective heat transfer coefficient (hi)	9.1 W·m^2·K
External convective heat transfer coefficient (he)	16.7 W·m^2·K
Porosity (%)	23
Wall thickness (e)	0.30 m
Initial temperature (T0)	293 K
Initial saturation (S0)	1
Absorbed solar flux (Φ0)	500 W·m^2

The wall was discretized with N = 500 nodes. Parameters are listed in Table 1.

3. RESULTS AND DISCUSSIONS

3.1 Experimental results

3.1.1 Dry bulk density and porosity

The physical parameters presented in Table 2 were compared with those reported in the literature in order to validate their consistency. The porosity accessible to water 33% is lower than that reported by the study by Li et al. [27], probably due to differences in the mineralogical composition and particle size of the material. The bulk density of 2040 kg·m³ was also studied [16].

Table 2. Presentation of physical parameter values for CSEB palm fibers reinforced

Physical Parameters	Value
Dry density (kg·m^3)	2040 ± 0.1
Water accessible porosity (%)	23 ± 0.1

3.1.2 Effect of moisture content on thermal properties

The experimental results, Figures 5-8, highlight the influence of water content on the thermal behavior of compressed stabilized, earth blocks reinforced with 0.05% palm fibers.

The relationship between thermal conductivity and moisture content is expressed. As shown in Figure 5, the thermal conductivity was measured by the box method. increases linearly from 0.46 to 1.19 W·m·K as the moisture content rises from 0% to 9.7% an increase of about 146%. The values obtained compared with analogous materials at comparable moisture contents lie above those reported by Meukam et al. [28] and below [10], probably due to differences in experimental conditions and in the materials tested.

Figure 6 shows that thermal diffusivity, determined by the flash method, increases by 69.39 % over the same interval, following a trend parallel to that of thermal conductivity. This concordance attests to the internal consistency of the measurements and gives values slightly higher than those reported in the study by Boulmaali and Belhamri [10] and Kabre et al. [12].

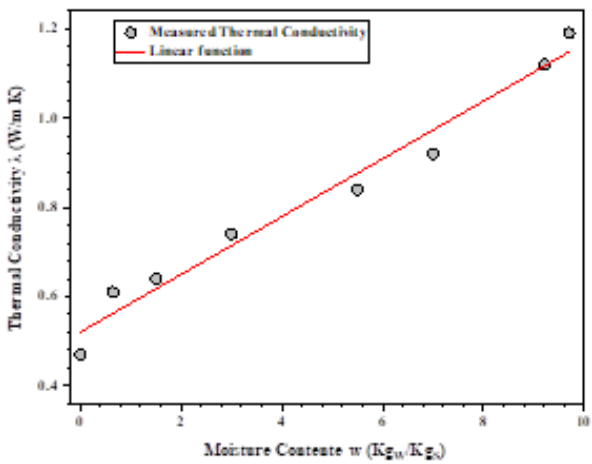

Figure 5. Thermal conductivity as a function of moisture content

In what follows, the specific heat capacity (C_p) and the thermal effusivity (E) are derived from the classical relations (25), (26) of transient heat conduction using the measured parameters thermal conductivity (λ) and thermal diffusivity (α), and density (ρ):

$$c_p = \frac{\lambda}{\rho\alpha} \tag{25}$$

$$\mathrm{E} = \sqrt{\rho\lambda c_p} \tag{26}$$

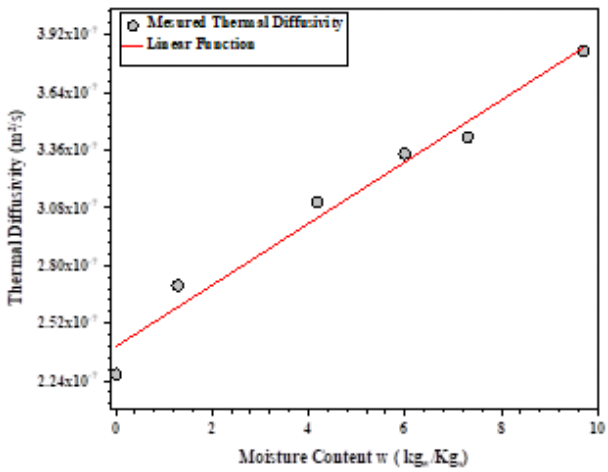

Figure 6. Thermal diffusivity as a function of moisture content

Figure 7 indicates an average 38.67% increase in mass-specific heat capacity, determined indirectly from the conductivity and diffusivity measurements; this trend remains consistent with the studies by Boulmaali and Belhamri [10] and Kabre et al. [12].

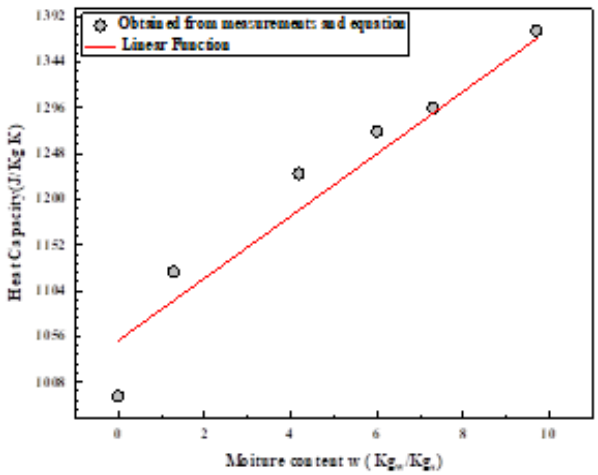

Figure 7. Thermal capacity as a function of moisture content

Figure 8 shows a marked rise in thermal effusivity, from 965 (J·m^2·K·s$^{1/2}$) to 1920.35 (J·m^2·K·s$^{1/2}$), which represents an increase close to 99% and reflects an enhanced ability of the material to exchange heat with its environment, in agreement with Kabre et al. [12].

These trends can be explained by the progressive replacement of air by water within the pores: Water, with its much higher thermal conductivity and mass-specific heat capacity, enhances both heat conduction and heat storage,

accounting for the observed increases. However, as the moisture content increases further, the thermal inertia may decrease due to faster propagation of heat fluxes, which can limit performance under strongly variable hygrometric conditions. Ultimately, explicit consideration of moisture content variability is essential for hygrothermal modeling and for the design of compressed, stabilized earth walls.

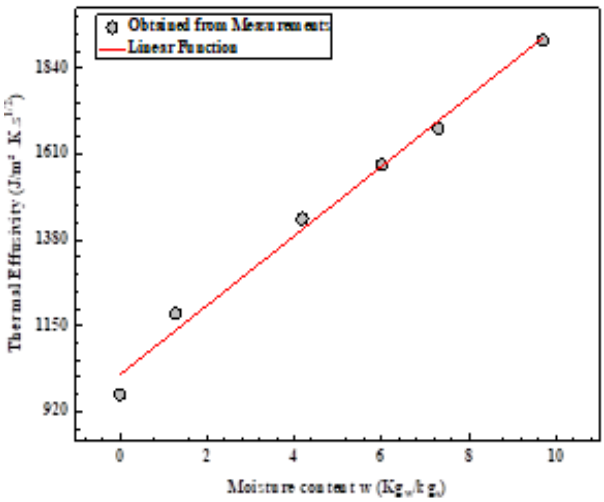

Figure 8. Thermal effusivity as a function of moisture content

3.1.3 Capillary water absorption of the palm fibers reinforced CSEBs

Figure 9 illustrates the evolution of water absorption per unit surface area as a function of the square root of time for the CSEB.

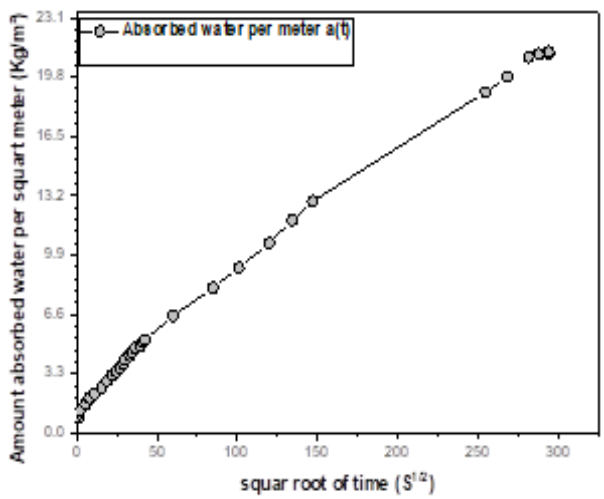

Figure 9. Evolution of the absorbed water per surface during the capillary absorption test for the palm fibers (CSEB)

3.2 Modeling results

3.2.1 Response of the wall under constant hygrothermal conditions–Case study 1

Case study 1 considers a vertical wall subjected to constant boundary conditions in terms of temperature and saturation, with convective exchanges and imposed mass fluxes on both faces, governed by vapor pressure gradients. It serves as a reference case to assess the evolution of coupled hygrothermal transfer under transient conditions.

The measured capillary absorption coefficient (a) is 0.14 $kg{\cdot}m^{-2}{\cdot}s^{-0.5}$, which is compared to the obtained results by Laou et al. [29] reported a lower value of 0.092 $kg.m^{-2}{\cdot}s^{-0.5}$.

While Kabre et al. [12] recorded a higher coefficient of 0.22 $kg{\cdot}m^{-2}{\cdot}s^{-0.5}$ for rammed earth samples, and the capillary moisture content (w_f) is measured 105 Kg/m^3 at Laou et al. [29].

Figure 10(a) shows the spatial distribution of the degree of saturation during drying. Saturation decreases slowly from the surface towards the interior, reflecting a diffusive drying front induced by the imposed mass flow.

Figure 10(b) shows the transient evolution of the temperature profile in a wall subjected to mixed boundary conditions, with constant and asymmetric convection coefficients. In the presence of a temperature difference (ΔT = 20 K), a net flow moves from the outside to the inside.

Initially, the temperature gradient varies greatly with position, and then gradually decreases as the material approaches the air temperature, reflecting a transition to a quasi-steady state; this dynamic is faster in the first few hours and then slows down. The achievement of thermal equilibrium remains closely linked to the stabilization of the degree of saturation.

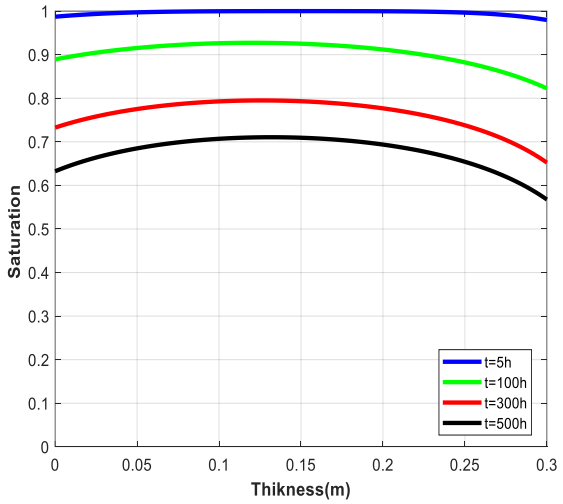

(a)

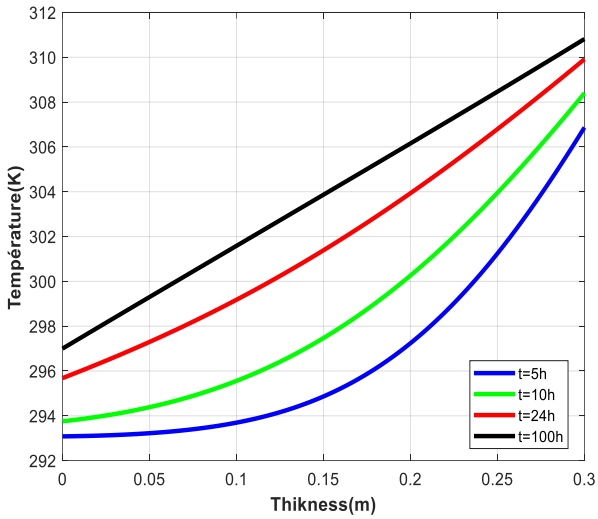

(b)

Figure 10. (a) Saturation distribution in the wall at different times, (b) temperature distribution in the wall at different times

Figures 11(a) and 11(b) illustrate the transient evolution of temperature and saturation at three points on the wall under constant conditions. The temperature increases more rapidly at the interfaces, while the center reacts more slowly due to thermal inertia. At the same time, saturation decreases monotonically with a delay at the center due to the diffusion of the drying front. This loss of moisture content locally reduces the effective thermal conductivity, thereby slowing down heat propagation. This interaction confirms the effect of hygrothermal coupling on thermal evolution despite the absence of external loading, as also observed by the study by Li et al. [27].

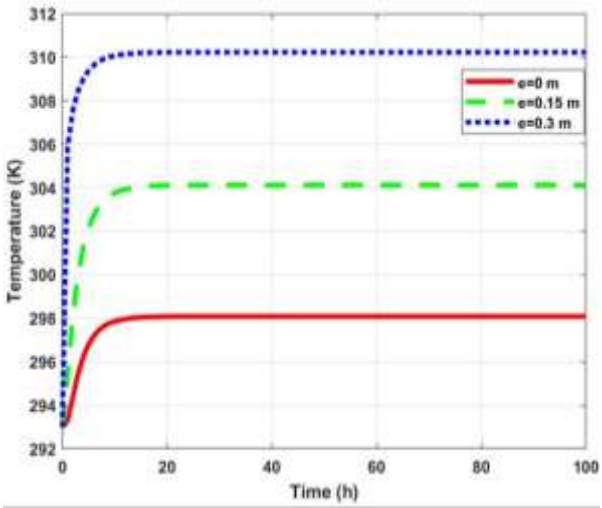

(a)

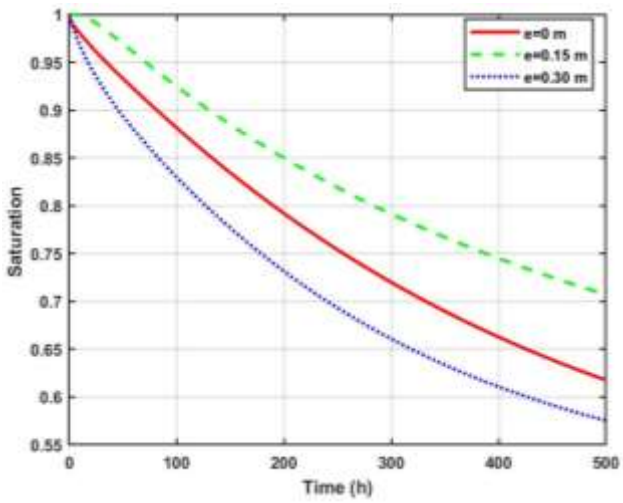

(b)

Figure 11. (a) Comparison of temperature profiles for different wall thickness under (constant boundary conditions), (b) comparison of saturation profiles for different wall thickness under (constant boundary conditions)

3.2.2 Response of the wall under periodic hygrothermal conditions without incident solar heat flux – Case study 2

Case study 2 considers sinusoidal variation of the exterior temperature, while moisture content transfer is still governed by vapor pressure gradients. This setup is used to investigate the wall's hygrothermal response to periodic thermal excitation in the absence of incident solar flux.

Figures 12(a) and 12(b) illustrate the evolution of temperature and water content at exterior, central, and interior positions of the wall, subjected to periodic ambient conditions without solar radiation. The temperature remains stable throughout the thickness, with a slight gradient at the interfaces and a damped response at the center, reflecting the thermal inertia of the material. Compared to the previous scenarios, however, the central thermal response is slightly faster. The water content decreases gradually, with sinusoidal oscillations visible on the surface after 24 hours, while the variation at the center remains more attenuated. This slow drying, induced by moisture diffusion, locally reduces thermal conductivity and slows down heat propagation. These interactions confirm, as reported by the study by Meukam et al. [28], the influence of hygrothermal coupling even in the absence of solar excitation.

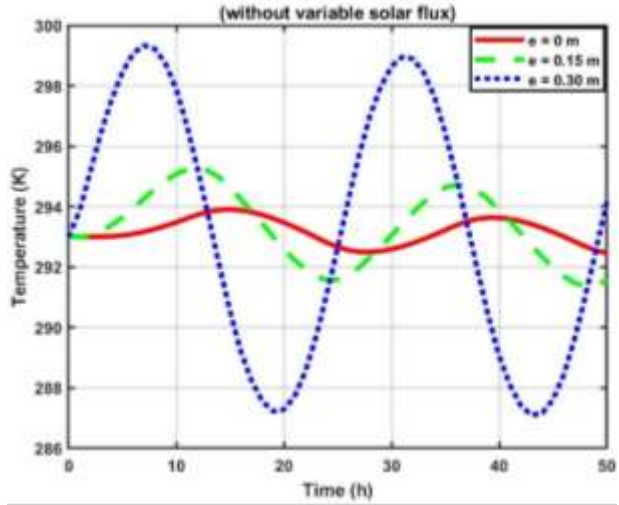

(a)

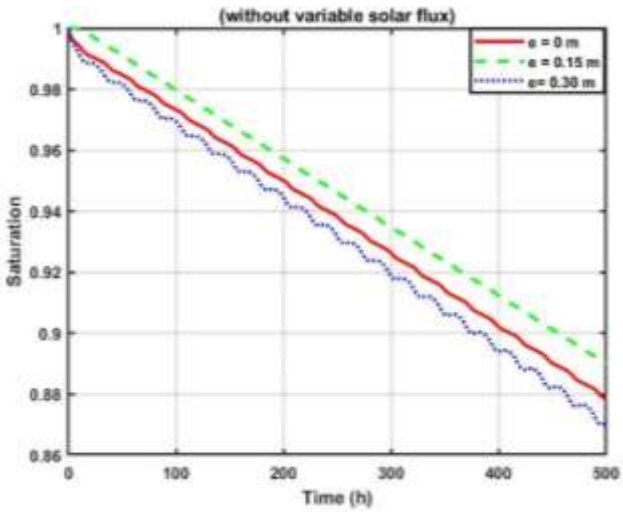

(b)

Figure 12. (a) Comparison of temperature profiles for different wall thickness under (variable boundary conditions), (b) comparison of saturation profiles for different wall thickness under (variable boundary conditions)

3.2.3 Response of the wall under periodic hygrothermal conditions with incident solar heat flux – Case study 3

Case study 3 considers the same periodic boundary conditions as the previous case, with the addition of an incident variable solar heat flux applied to the exterior surface. This configuration allows for evaluating the combined effect of ambient temperature variations and solar irradiation on the coupled hygrothermal behavior of the wall.

Figures 13(a) and 13(b) show the temporal evolution of temperature and saturation at the exterior (exposed to solar radiation) and interior positions of the wall. At the exterior, solar input induces a rapid temperature rise accompanied by a progressive decrease in saturation, reflecting accelerated drying of the material. Compared with the case without radiation, temperature and saturation gradients are markedly amplified at the interfaces. The surface curves display more pronounced variations, indicating stronger hygrothermal coupling and intensified drying dynamics. These results confirm the direct influence of solar excitation on the hygrothermal behavior of the material, in agreement with the findings of studies by Tamene et al. [30], who demonstrated that solar flux amplifies heat transfer and modifies the oscillatory dynamics in building materials under coupled heat and mass transfer conditions. Similarly, Škerget et al. [31] investigated, through transient simulations, coupled heat and moisture transport in a homogeneous single-layer porous wall subjected to a sinusoidal outdoor air temperature and a diurnal solar heat flux (zero at night and sinusoidal during daytime). They reported a pronounced near-surface response to the external forcing, with a rapid attenuation of its influence with depth; furthermore, the moisture content at the internal surface was essentially unaffected by the external moisture variation.

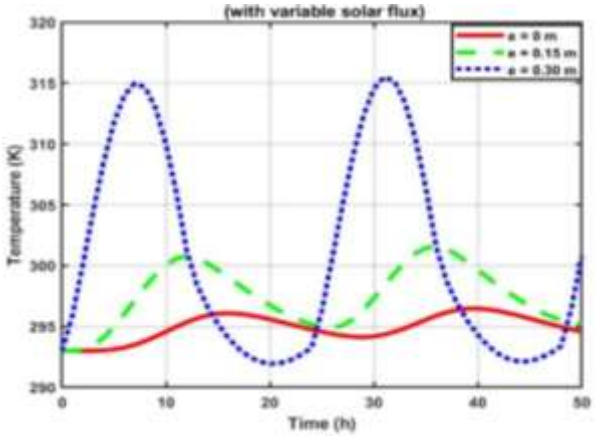

(a)

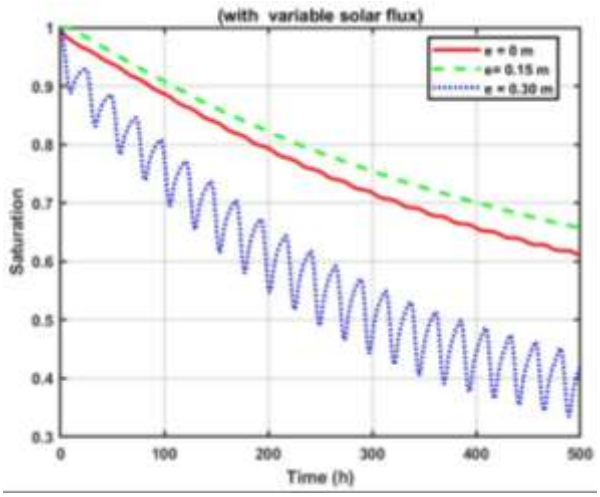

(b)

Figure 13. (a) Comparison of temperature profiles for different wall thickness under (variable boundary conditions and variable incident flux), (b) comparison of saturation profiles for different wall thickness under (variable boundary conditions and variable incident flux)

4. CONCLUSION

This study successfully employed a complementary experimental and numerical approach to investigate the hygrothermal behavior of CSEB reinforced with a low content (0.05%) of palm fibers. The research provides crucial, previously lacking insights into the thermal properties and hygrothermal performance of this specific formulation, thereby enhancing the understanding of this eco-friendly building material for sustainable construction.

Measurements performed as a function of moisture content enabled the determination of the material's hygrothermal properties and the assessment of its internal transfer mechanisms under various climatic conditions.

Experimental results showed that thermal conductivity ranged from 0.46 to 1.19 W·m·K, while thermal diffusivity varied between 2.27×10^{-7} and 3.84×10^{-7} $m^2 \cdot s$ for moisture contents between 0 and 9.7%. The capillary absorption coefficient, 0.14 $kg \cdot m^{-2} \cdot s^{-1/2}$, reflects moderate imbibition capacity typical of porous earthen materials. Furthermore, numerical simulations reproduced the spatio-temporal evolution of temperature and saturation fields within the single-layer wall, revealing the significant influence of moisture on heat distribution and the coupled heat and moisture transport processes within the material. The temperature profiles indicate a thermal inertia favorable to the use of this eco-building material in arid and semi-arid climates. Indeed, the reduced temperature range and the difference between indoor and outdoor temperatures are advantages to be exploited in bioclimatic building strategies.

In this context, this work provides a robust methodological contribution to the characterization of the coupled hygrothermal behavior of stabilized compressed earth materials and establishes a reference framework for predictive modeling and optimization of bio-based envelopes designed for hot and arid climates.

REFERENCES

[1] International Energy Agency (IEA). (2019). World Energy Outlook. https://www.iea.org/reports/world-energy-outlook-2019.

[2] International Energy Agency (IEA). (2018). The Future of Cooling: Opportunities for energy-efficient air conditioning. https://www.iea.org/reports/the-future-of-cooling.

[3] Kharchi, R. (2013). Energy efficiency in buildings. Bulletin of the CDER (Renewable Energy Development Center), Algiers, No. 028. https://www.cder.dz/vlib/bulletin/pdf/bulletin_028_05.pdf.

[4] Boudghene Stambouli, A. (2011). Promotion of renewable energies in Algeria: Strategies and perspectives. Renewable and Sustainable Energy Reviews, 15(2): 1169-118. https://doi.org/10.1016/j.rser.2010.11.017

[5] Benhelal, E., Zahedi, G., Shamsaei, E., Bahadori, A. (2013). Global strategies and potentials to curb CO_2 emissions in cement industry. Journal of Cleaner Production, 51: 142-161. https://doi.org/10.1016/j.jclepro.2012.10.049

[6] Arduin, D., Caldas, L.R., Paiva, R.d.L.M., Rocha, F. (2022). Life cycle assessment (LCA) in earth

construction: A systematic literature review considering five construction techniques. Sustainability, 14(20): 13228. https://doi.org/10.3390/su142013228
[7] Cagnon, H., Aubert, A., Morel, J.C., Chevalier, M. (2014). Hygrothermal properties of earth bricks. Energy and Buildings, 80: 208-217. https://doi.org/10.1016/j.enbuild.2014.05.024
[8] Bruno, A.W., Perlot, C., Mendes, J., Gallipoli, D. (2018). A microstructural insight into the hygro-mechanical behaviour of a stabilised hypercompacted earth. Materials and Structures, 51(1): 32. https://doi.org/10.1617/s11527-018-1160-9
[9] Ndjeumi, C.C., Djomou, D.P.N., Nkeng, G.E., Souaibou, F.A., Anong, S. (2024). Assessment of cement-lime as stabilizer on mud bricks. Journal of Materials Science and Chemical Engineering, 12(7): 1-13. https://doi.org/10.4236/msce.2024.127001
[10] Boulmaali, M., Belhamri, A. (2023). Investigation of thermal inertia and hydric properties of an eco-building material: Compressed stabilized earth blocks. Heat and Mass Transfer, 59(3): 713-727. https://doi.org/10.1007/s00231-022-03292-1
[11] Saidi, M., Cherif, A.S., Sediki, E., Zeghmati, B. (2020). Hygrothermal behavior of earth-based materials: Experimental and numerical analysis. MATEC Web of Conferences, 330: 01030. https://doi.org/10.1051/matecconf/202033001030
[12] Kabre, S., Ouedraogo, F., Naon, B., Messan, A., Benet, J.C., Zougmoré, F. (2019). Evaluation of the thermo-hydro-mechanical properties of compressed earth bricks (CEB) from the Matourkou quarry, Burkina Faso. Afrique SCIENCE, 15(3): 12-22. https://www.afriquescience.net/admin/postpdfs/eec43027a0cb57c11a5c812f817e5fb01729215771.pdf.
[13] Nagaraj, H.B., Sravan, M.V., Arun, T.G., Jagadish, K.S. (2014). Role of lime with cement in long-term strength of Compressed Stabilized Earth Blocks. International Journal of Sustainable Built Environment, 3(1): 54-61. https://doi.org/10.1016/j.ijsbe.2014.03.001
[14] Ezbakhe, H., Bousad, S., El Bakkour, A., Ajzoul, T., El Bouardi, A. (2011). Thermal study of cement-stabilized earth used in construction in northern Morocco. Revue Énergie Renouvelable, Thermal Days, 69-72.
[15] Nkotto, L.I.N.N., Kamgang, G.D., Tiewa, J., Kanda, J.S., Loweh, S.S., Likiby, B. (2020). Characterization of blocks produced by adding coconut fibers to laterite–cement-based construction materials. Afrique SCIENCE, 17(4): 170-184. https://www.afriquescience.net/admin/postpdfs/1b753aed4ecac0e94c7affaca16b6f8a1728410102.pdf.
[16] Taallah, B., Guettala, A., Guettala, S., Kriker, A. (2014). Mechanical properties and hygroscopicity behavior of compressed earth block filled by date palm fibers. Construction and Building Materials, 59: 161-168. https://doi.org/10.1016/j.conbuildmat.2014.02.058
[17] Djoudi, A., Khenfer, M.M., Bali, A., Bouziani, T. (2014). Effect of the addition of date palm fibers on thermal properties of plaster concrete: Experimental study and modeling. Journal of Adhesion Science and Technology, 28(20): 2100-2111. https://doi.org/10.1080/01694243.2014.948363
[18] ISO. (2016). Hygrothermal performance of building materials and products – Determination of thermal properties of porous materials using the box method (ISO 16957:2016). Geneva: International Organization for Standardization.
[19] Vozár, L., Hohenauer, W. (2003). Flash method of measuring thermal diffusivity – A review. High Temperatures – High Pressures, 36(3): 253-264. https://doi.org/10.1068/htjr119
[20] Philip, J.R., De Vries, D.A. (1957). Moisture movement in porous materials under temperature gradients. Eos, Transactions American Geophysical Union, 38(2): 222-232. https://doi.org/10.1029/TR038i002p00222
[21] Degiovanni, A., Laurent, M. (1986). A new technique for identifying thermal diffusivity using the flash method. Revue de Physique Appliquée, 21(3): 229-237. https://doi.org/10.1051/rphysap:01986002103022900
[22] Bories, S. (1982). Heat and mass transfer in materials: A critical analysis of the different mathematical models used. In Moisture in Buildings (UNESCO Seminar), France, pp. 13-32.
[23] Fauconnier, R. (1982). Influence of humidity on the energy consumption of a building under intermittent heating (Modeling and coupling of phenomena). In Moisture in Buildings (UNESCO Seminar), pp. 147-186.
[24] Bird, R.B., Stewart, W.E., Lightfoot, E.N. (2006). Transport Phenomena (Revised 2nd ed.). John Wiley & Sons, Inc., pp. 928.
[25] Patankar, S.V. (1980). Numerical Heat Transfer and Fluid Flow. Hemisphere Publishing Corporation.
[26] Crausse, P., Laurent, J.P., Perrin, B. (1996). Influence des phénomènes d'hystérésis sur les propriétés hydriques de matériaux poreux: Comparaison de deux modèles de simulation du comportement thermohydrique de parois de bâtiment. Revue générale de Thermique, 35(410): 95-106. https://doi.org/10.1016/S0035-3159(96)80002-X
[27] Li, C., Li, K., Chen, Z. (2008). Numerical analysis of moisture influential depth in concrete and its application in durability design. Tsinghua Science & Technology, 13(S1): 7-12. https://doi.org/10.1016/S1007-0214(08)70119-6
[28] Meukam, P., Jannot, Y., Noumowe, A., Kofane, T.C. (2004). Thermo physical characteristics of economical building materials. Construction and Building Materials, 18(6): 437-443. https://doi.org/10.1016/j.conbuildmat.2004.03.010
[29] Laou, L., Aubert, J.E., Yotte, S., Maillard, P., Ulmet, L. (2021). Hygroscopic and mechanical behaviour of earth bricks. Materials and Structures, 54(3): 116. https://doi.org/10.1617/s11527-021-01701-1
[30] Tamene, Y., Abboudi, S., Bougriou, C. (2011). Study of heat and moisture diffusion through a wall exposed to solar heat flux. Journal of Engineering Science and Technology, 6(4): 429-444.
[31] Škerget, L., Tadeu, A., Brebbia, C. A. (2018). Transient simulation of coupled heat and moisture flow through a multi-layer porous solidexposed to solar heat flux. International Journal of Heat and Mass Transfer, 117: 273-279. https://doi.org/10.1016/j.ijheatmasstransfer.2017.10.010

NOMENCLATURE

L	characteristic length, m
l	width, m
e	thikness, m

A	area, m^2
x	coordinate, m
T	temperature, K
C_P	specific heat, J·kg·K
E	thermal effusivity, $J \cdot m^2 \cdot K^1 \cdot s^{1/2}$
Q	heat flux, W. m^{-2}
M	mass, kg
h_m	convective mass transfer coefficient, $m \cdot s^{-1}$
q_m	moisture mass flux, $kg/m^2 \cdot s$
D	mass diffusivity, $m^2 \cdot s^{-1}$
S	saturation
W	moisture content, kg_w/kg_s
A	capillary absorption coefficient, $kg \cdot m^{-2} \cdot s^{0.5}$
P_v	vapor pressure, Pa
Sh	Sherwood number, dimensionless
t	time, s

Greek symbols

α	thermal diffusivity, $m^2 \cdot s^1$
λ	thermal conductivity, W/m·K
φ	relative humidity
Φ	absorbed solar flux, $W \cdot m^2$
ρ	density of the fluid, $kg \cdot m^3$
ε	porosity, volumetric fraction
τ	time lag, s

Subscripts

0	initial
s	dry solid
L	liquid
f	free water
h	Humid solid
sat	saturation
v	vapor
Sufi	the interior surface
Sufe	the exterior surface
i	interior
e	exterior
*	effective

Abbreviation

CSEB	compressed stabilized earth block